


Positive cross-correlated shot noise and quasibound states in an NSNSN geometryCorey Ostrove and Linda Reichl *Center for Complex Quantum Systems, The University of Texas at Austin, Austin, Texas 78712, USA*

(Received 14 July 2020; revised 2 June 2021; accepted 3 June 2021; published 15 June 2021)

Solid-state superconducting heterostructures can provide a possible source of entangled electrons for the purpose of quantum-information processing, and shot noise can indicate when this occurs. Shot noise cross-correlations in a ballistic NSNSN (normal-superconductor-normal-superconductor-normal) is normally negative for electron currents, but becomes positive for entangled electrons that result from the breakup of Cooper pairs. A one-to-one correspondence is found between the energies of the quasibound states and regions of positivity in the cross-correlated shot noise. The quasibound states of the NSNSN system are associated with poles of the NSNSN scattering matrix. We find that regions of positive cross-correlated shot noise distributions, and the associated emission of entangled electrons, exist over a wide range of system sizes and in the presence of multiple quasibound states. We also find that, at the quasibound-state energies, the Andreev approximation is not adequate to describe the key physical processes in the NSNSN device.

DOI: [10.1103/PhysRevB.103.224518](https://doi.org/10.1103/PhysRevB.103.224518)**I. INTRODUCTION**

The potential for superconductors to serve as a source of entangled electron pairs in solid-state devices has led to a resurgence in interest in the study of superconducting heterostructures in recent years [1–5]. The key observation is that the Cooper pairs underlying superconductivity naturally form maximally entangled pairs of electrons, which if spatially separated (say in separate leads of a superconducting heterostructure) would enable these electrons to be used for quantum-information processing tasks. Superconducting heterostructures designed with this purpose in mind are referred to as Cooper pair splitters (CPS).

Cooper pair splitters and superconducting heterostructures more generally have also been studied in the context of superconducting spintronics devices [6–8], where they are considered as potential sources of spin-polarized electronic currents within some larger superconducting hybrid system. This application is particularly relevant for the development of spintronic-based quantum dot qubits, and was proposed early on as a source of nonlocal electronic entanglement in these devices [9]. Recent theoretical work has extended this line of research to the spin-polarization of thermoelectric currents within hybrid superconductor-ferromagnetic systems [10].

One of the key limitations to realizing superconductors as an entanglement source is the efficiency with which Cooper pairs can be separated into spatially nonlocal leads in a given superconducting heterostructure [11,12]. A substantial amount of theoretical work has been done to characterize the nonlocal transport properties of NSN (normal-superconductor-normal) geometries as they relate to the design of CPS [2,3,13–15]. Also, a number of experimental groups have demonstrated CPS in a number of different architectures, some with rather high efficiencies [4,16,17]. Most CPS research has been focused on standard BCS-type superconductors, but some theory has also been worked out for systems with anisotropic order parameters [1,18], and

for structures which incorporate quantum Hall edge channels [19].

The main scattering process responsible for the generation of entanglement in CPS devices is crossed Andreev reflection (CAR) [11,20–22]. Crossed Andreev reflection is a scattering process in which an incident particle (hole) is transmitted as a hole (particle) on the other side of the system. Much of the existing research on CPS has focused on designing architectures that enhance the prevalence of CAR. Proposals include using double quantum dots (QD) [3,16,23], spin filtering using ferromagnetic leads [22], anomalous scattering in graphene [24–26] and energy filtering in semiconductors [2]. Experimentally, extensive progress has been made with QD based devices [17,27]. Additionally, these proposals are not necessarily mutually exclusive, and theoretical and experimental progress has been made with CPS devices that use a combination of double QD and either ferromagnetic leads or external magnetic fields [28–32].

The generation of entanglement in CPS devices is known to be related to the positivity of the cross-correlated shot noise, as obtained from measurements of the nonlocal current-current correlations between different leads [11]. In the sections below we adopt this perspective and investigate the cross-correlated shot noise for the NSNSN (normal-superconductor-normal-superconductor-normal) geometry, shown in Fig. 1. We make use of a scattering theory approach using the Bogoliubov-de Gennes equations [33]. Our methods are adapted from the techniques introduced by Demers and Griffin, and Blonder, Tinkham and Klapwijk (BTK) [33–35]. We obtain results for the scattering matrix of the system without the Andreev approximation, and use the scattering matrix to probe the relationship between long-lived quasibound states in the system and positive regions of the cross-correlated shot noise energy distribution.

Using the BTK approach we find that there is a one-to-one correspondence between the energies of the quasibound states

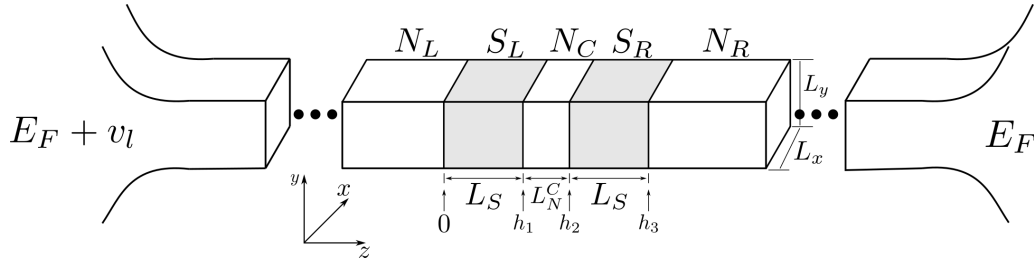


FIG. 1. NSNSN geometry studied in this paper. The left and right leads are much longer than the central SNS region and are connected to thermal reservoirs with Fermi energy E_F with an additional bias of v_l applied to the left lead. More details on the system parameters used can be found in Sec. IV and Table I.

and the regions of positivity in the cross-correlated shot noise energy distribution. We also find that this connection is robust and persists in the presence of multiple quasibound states and for a wide range of system sizes. Moreover we analyze the noise cross-correlations for the NSN geometry and find that, in contrast to the NSNSN geometry, the total cross-correlated shot noise distribution remains negative over the entire sub-gap energy range of the system. The results for the NSNSN geometry using the full scattering theory are compared to those obtained using the Andreev approximation and we find that there is a large deviation between the behavior of the cross-correlations at the quasibound state energies. The basis of the Andreev approximation is dropping higher order terms in the ratio of the superconducting gap energy Δ_0 and the Fermi energy E_F from the Bogoliubov-de Gennes equations. Our use of the superconductor LSCO as our model material in the numerics presented in this paper amplifies the differences observed between the full scattering theory and the Andreev approximation in the cross-correlated shot noise distributions because it has a relatively large value of Δ_0/E_F .

The paper is organized as follows. In Sec. II, we derive the scattering matrix for the NSNSN system. In Sec. III, we write the expressions for the cross-correlated shot noise in terms of the scattering matrix elements. In Sec. IV we list the properties of LSCO, the high- T_c superconductor that is used in our analysis, and discuss the rationale for using that material. In Sec. V we present results for the cross-correlated shot noise energy distributions, and in Sec. VI we describe the behavior of the scattering amplitudes. In Sec. VII we focus on the resonances in the scattering coefficients and the connection between the quasibound states and the positive peaks in the cross-correlated shot noise energy distribution. In Sec. VIII, we break down the dominant contributions to the positive cross-correlated shot noise at the resonances in our system.

TABLE I. System parameters for LSCO, taken from [38], Table 7.4.

T_c (K)	38
ξ (a_B)	65
Δ (E_H)	0.000212
E_F (E_H)	0.000935
ϵ_{\max} (E_H)	0.000356
T_0 (K)	16.3
L_y	1.85ξ
L_x	$1.2L_y$

In Sec. IX, we compare the results for the NSNSN system to those of the NSN geometry and we also look at the system size dependence of the NSNSN geometry. In Sec. XI, we compare the results of the full scattering theory used throughout this paper to those obtained using the Andreev approximation. Finally, in Sec. XII we will summarize our results.

II. SCATTERING THEORY

In this section we provide a brief overview of the scattering theory techniques used to analyze the NSNSN system.

The wave functions in the left lead (N_L) and right lead (N_R) consist of superpositions of incoming and outgoing particles and holes, confined to the first propagating channel of the waveguide, as shown diagrammatically in Fig. 2. In the superconducting regions we use energy eigenfunctions from the Bogoliubov-de Gennes equations (BdG) for those regions (see Appendix A). We then can apply basic scattering theory in order to derive the scattering matrix for NSNSN system.

We begin by writing down the wave functions in each of the five regions:

$$\begin{aligned}
 \psi_{N_\alpha}(z) &= \frac{A_{N_\alpha}^p}{\sqrt{q_p^\alpha}} \begin{pmatrix} 1 \\ 0 \end{pmatrix} e^{iq_p^\alpha z} + \frac{B_{N_\alpha}^h}{\sqrt{q_h^\alpha}} \begin{pmatrix} 0 \\ 1 \end{pmatrix} e^{-iq_h^\alpha z} \\
 &+ \frac{C_{N_\alpha}^p}{\sqrt{q_p^\alpha}} \begin{pmatrix} 1 \\ 0 \end{pmatrix} e^{-iq_p^\alpha z} + \frac{D_{N_\alpha}^h}{\sqrt{q_h^\alpha}} \begin{pmatrix} 0 \\ 1 \end{pmatrix} e^{+iq_h^\alpha z}, \\
 \psi_{S_\alpha}(z) &= \frac{A_{S_\alpha}^p}{\sqrt{k_p^\alpha}} \begin{pmatrix} u_o \\ v_o \end{pmatrix} e^{ik_p^\alpha z} + \frac{B_{S_\alpha}^h}{\sqrt{k_h^\alpha}} \begin{pmatrix} v_o \\ u_o \end{pmatrix} e^{-ik_h^\alpha z} \\
 &+ \frac{C_{S_\alpha}^p}{\sqrt{k_p^\alpha}} \begin{pmatrix} u_o \\ v_o \end{pmatrix} e^{-ik_p^\alpha z} + \frac{D_{S_\alpha}^h}{\sqrt{k_h^\alpha}} \begin{pmatrix} v_o \\ u_o \end{pmatrix} e^{+ik_h^\alpha z}. \quad (1)
 \end{aligned}$$

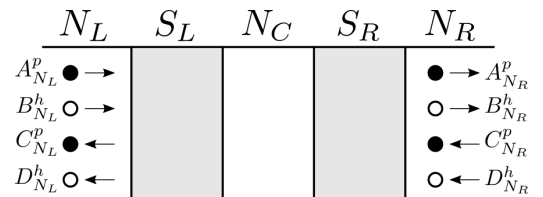


FIG. 2. Incoming and outgoing particles and holes in the left and right leads along with the labels corresponding to Eq. (3). Solid circles represent electrons and open circles represent holes.

We have introduced the placeholder α , with $\alpha \in \{L, C, R\}$ for the normal regions and $\alpha \in \{L, R\}$ for the superconductors. The normalization factors for each of the terms in Eq. (1) ensure that our system carries unit current [36]. The coherence factors u_0 and v_0 , and the wave vectors k_p^α , k_h^α , q_p^α , and q_h^α are given in Appendix A. We are working in the high-transparency limit, so we require that the wave functions in Eq. (1) and their derivatives are continuous at the interfaces between the normal regions and superconductors. The explicit boundary conditions are

$$\begin{aligned} \psi_{N_L}(0) &= \psi_{S_L}(0), & \psi_{S_L}(h_1) &= \psi_{N_C}(h_1), \\ \psi_{N_C}(h_2) &= \psi_{S_R}(h_2), & \psi_{S_R}(h_3) &= \psi_{N_R}(h_3), \\ \dot{\psi}_{N_L}(0) &= \dot{\psi}_{S_L}(0), & \dot{\psi}_{S_L}(h_1) &= \dot{\psi}_{N_C}(h_1), \\ \dot{\psi}_{N_C}(h_2) &= \dot{\psi}_{S_R}(h_2), & \dot{\psi}_{S_R}(h_3) &= \dot{\psi}_{N_R}(h_3). \end{aligned} \quad (2)$$

These boundary conditions give us a system of 16 equations, which we can use to eliminate the coefficients for the S_L , N_C , and S_R regions. Once we have eliminated the three central regions we can write the coefficients corresponding to outgoing particles and holes in terms of the coefficients of incoming particles and holes. Doing so we obtain the scattering matrix of the system,

$$\begin{pmatrix} C_{N_L}^p \\ D_{N_L}^h \\ A_{N_R}^p \\ B_{N_R}^h \end{pmatrix} = \begin{pmatrix} r_{pp}^{LL} & r_{ph}^{LL} & t_{pp}^{LR} & t_{ph}^{LR} \\ r_{hp}^{LL} & r_{hh}^{LL} & t_{hp}^{LR} & t_{hh}^{LR} \\ t_{pp}^{RL} & t_{ph}^{RL} & r_{pp}^{RR} & r_{ph}^{RR} \\ r_{hp}^{RL} & r_{hh}^{RL} & r_{hp}^{RR} & r_{hh}^{RR} \end{pmatrix} \begin{pmatrix} A_{N_L}^p \\ B_{N_L}^h \\ C_{N_R}^p \\ D_{N_R}^h \end{pmatrix}. \quad (3)$$

The scattering matrix elements are all functions of the energy of the particles and holes, and the phase difference between the superconducting regions ϕ . The subscripts on the scattering elements denote the outgoing and incoming excitation types, respectively, and the superscripts denote the outgoing and incoming leads, respectively.

A common approximation made when studying scattering through superconducting heterostructures is the Andreev approximation [37]. By including the boundary conditions on the derivatives of the wave functions, we are working outside

of the Andreev approximation. A more detailed discussion of this point can be found in Sec. XI. The analytical expressions for the full scattering coefficients, without the Andreev approximation, are far too long to include in print, so we will be focusing mainly on numerical results in the following sections.

III. CROSS-CORRELATED SHOT NOISE

Given the field operator, $\hat{\psi}_{N_L}(z, t)$ for the left lead (see Appendix A), we can write the corresponding current operator for the left lead using the relation

$$\hat{J}_L(z, t) = \frac{\hbar e_c}{2im} \left(\hat{\psi}_{N_L}^\dagger(z, t) \frac{d\hat{\psi}_{N_L}(z, t)}{dz} - \frac{d\hat{\psi}_{N_L}^\dagger(z, t)}{dz} \hat{\psi}_{N_L}(z, t) \right), \quad (4)$$

where e_c is the electron charge and m is the effective mass of electrons in the left lead. The cross-correlated shot noise is the symmetrized correlation function for fluctuations about the average current at different times and between the left and right leads,

$$\begin{aligned} S^{LR}(z, y; t, s) &= \frac{1}{2} (\langle \hat{J}_L(z, t) \hat{J}_R(y, s) \rangle - \langle \hat{J}_L \rangle \langle \hat{J}_R \rangle) \\ &\quad + (\langle \hat{J}_R(y, s) \hat{J}_L(z, t) \rangle - \langle \hat{J}_R \rangle \langle \hat{J}_L \rangle), \end{aligned} \quad (5)$$

where $\langle \cdot \rangle$ is the thermal average. Due to its connection to entanglement generation, the main quantity of interest here is the zero-frequency limit of the Fourier transformed cross-correlated shot noise [11], which we write as

$$S_{tot}^{LR} \equiv \int de dS^{LR}(e) = S_{pp}^{LR} + S_{hh}^{LR} + S_{ph}^{LR}. \quad (6)$$

S_{tot}^{LR} naturally decomposes into three components, S_{pp}^{LR} , S_{hh}^{LR} , and S_{ph}^{LR} , which are respectively the contributions due to correlations between particles in the left and right leads, holes in the left and right leads, and between particles in the left lead and holes in the right lead (and vice versa), respectively. The expressions for S_{pp}^{LR} , S_{hh}^{LR} , and S_{ph}^{LR} in terms of the scattering matrix elements can be written as

$$\begin{aligned} S_{pp}^{LR} &= \frac{m_L m_R}{\pi^2 \hbar^4} \int de [F_p^L N_p^L ((- |r_{hp}^{LL}|^2 + |r_{pp}^{LL}|^2 - 1) (- |t_{hp}^{LR}|^2 + |t_{pp}^{LR}|^2)) + F_p^R N_p^R ((- |r_{hp}^{RR}|^2 + |r_{pp}^{RR}|^2 - 1) (- |t_{hp}^{LR}|^2 + |t_{pp}^{LR}|^2)) \\ &\quad + (F_p^L N_p^R + F_p^R N_p^L) (\text{Re}[r_{hp}^{LL} r_{hp}^{RR} t_{hp}^{LR*} t_{hp}^{RL*}] - \text{Re}[r_{hp}^{LL*} r_{pp}^{RR*} t_{pp}^{RL} t_{hp}^{LR}] + \text{Re}[r_{pp}^{LL} r_{pp}^{RR} t_{pp}^{LR*} t_{pp}^{RL*}] - \text{Re}[r_{pp}^{LL*} r_{hp}^{RR*} t_{hp}^{RL} t_{pp}^{LR}])], \end{aligned} \quad (7)$$

$$\begin{aligned} S_{hh}^{LR} &= \frac{m_L m_R}{\pi^2 \hbar^4} \int de [F_h^L N_h^L ((|r_{hh}^{LL}|^2 - |r_{ph}^{LL}|^2 - 1) (|t_{hh}^{LR}|^2 - |t_{ph}^{LR}|^2)) + F_h^R N_h^R ((|r_{hh}^{RR}|^2 - |r_{ph}^{RR}|^2 - 1) (|t_{hh}^{LR}|^2 - |t_{ph}^{LR}|^2)) \\ &\quad + (F_h^L N_h^R + F_h^R N_h^L) (\text{Re}[r_{hh}^{LL} r_{hh}^{RR} t_{hh}^{LR*} t_{hh}^{RL*}] - \text{Re}[r_{hh}^{LL*} r_{ph}^{RR*} t_{ph}^{RL} t_{hh}^{LR}] + \text{Re}[r_{ph}^{LL} r_{ph}^{RR} t_{ph}^{LR*} t_{ph}^{RL*}] - \text{Re}[r_{ph}^{LL*} r_{hh}^{RR*} t_{hh}^{RL} t_{ph}^{LR}])], \end{aligned} \quad (8)$$

$$\begin{aligned} S_{ph}^{LR} &= \frac{m_L m_R}{\pi^2 \hbar^4} \int de [(F_h^L N_p^L + F_p^L N_h^L) (\text{Re}[r_{hh}^{LL} r_{hp}^{LL*} t_{hp}^{RL} t_{hh}^{RL*}] - \text{Re}[r_{hh}^{LL} r_{hp}^{LL*} t_{ph}^{RL*} t_{pp}^{RL}] - \text{Re}[r_{ph}^{LL} r_{pp}^{LL*} r_{hh}^{RL*} t_{hp}^{RL}] + \text{Re}[r_{ph}^{LL} r_{pp}^{LL*} t_{pp}^{RL} r_{ph}^{RL*}]) \\ &\quad + (F_h^R N_p^R + F_p^R N_h^R) (\text{Re}[r_{hh}^{RR} r_{hp}^{RR*} t_{hp}^{LR} t_{hh}^{LR*}] - \text{Re}[r_{hh}^{RR} r_{hp}^{RR*} t_{ph}^{LR*} t_{pp}^{LR}] - \text{Re}[r_{ph}^{RR} r_{pp}^{RR*} t_{hh}^{LR*} t_{hp}^{LR}] + \text{Re}[r_{ph}^{RR} r_{pp}^{RR*} t_{pp}^{LR} t_{ph}^{LR*}]) \\ &\quad + (F_h^L N_p^R + F_p^L N_h^L) (\text{Re}[r_{hh}^{LL} r_{hp}^{RR} t_{hp}^{LR*} t_{hh}^{RL*}] - \text{Re}[r_{hh}^{LL*} r_{pp}^{RR*} t_{ph}^{RL} t_{hp}^{LR}] + \text{Re}[r_{ph}^{LL} r_{pp}^{RR} t_{pp}^{LR*} t_{ph}^{RL*}] - \text{Re}[r_{ph}^{LL*} r_{hp}^{RR*} t_{hh}^{RL} t_{pp}^{LR}]) \\ &\quad + (F_p^L N_h^R + F_h^R N_p^L) (\text{Re}[r_{hp}^{LL} r_{hh}^{RR} t_{hh}^{LR*} t_{hp}^{RL*}] - \text{Re}[r_{hp}^{LL*} r_{ph}^{RR*} t_{pp}^{RL} t_{hh}^{LR}] + \text{Re}[r_{pp}^{LL} r_{ph}^{RR} t_{ph}^{LR*} t_{pp}^{RL*}] - \text{Re}[r_{pp}^{LL*} r_{hh}^{RR*} t_{hp}^{RL} t_{ph}^{LR}])]. \end{aligned} \quad (9)$$

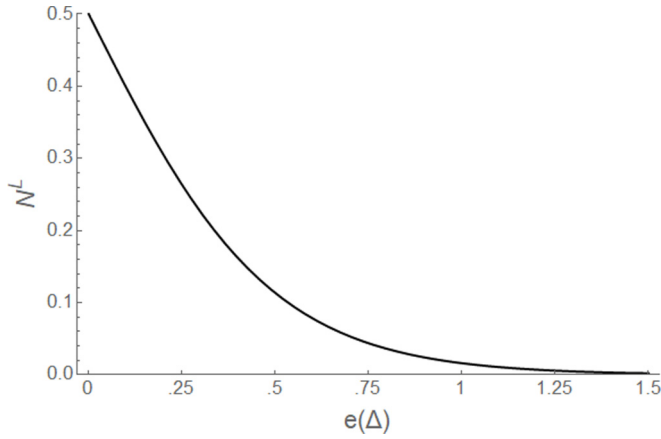


FIG. 3. Plot of the Fermi distribution, N^L , with zero bias and $T_0 = 16.3$ K.

In the above expressions $N_\gamma^\alpha = \langle \hat{a}_{e,\gamma}^{\alpha\dagger} \hat{a}_{e,\gamma}^\alpha \rangle = (1 + e^{\beta(e + \text{sgn}(\gamma)v_\alpha)})^{-1}$, is the Fermi distribution for the thermal reservoir of excitations of type γ connected to lead α , where $\gamma \in \{p, h\}$. β is the standard inverse temperature parameter $\beta = \frac{1}{k_B T}$, with k_B being the Boltzmann constant and T the temperature of the system. We define $\text{sgn}(\gamma) = +1$ for $\gamma = p$, $\text{sgn}(\gamma) = -1$ for $\gamma = h$ and $F_\gamma^\alpha = 1 - N_\gamma^\alpha$. Due to the convention we have adopted of assigning holes positive energy, at zero bias both electrons and holes have the same thermal distributions, but are shifted in opposite directions in the presence of an applied bias [18]. The quantities dS_α^{LR} give the energy distributions of these terms.

IV. SYSTEM PARAMETERS

For our model system we use parameters based on the high- T_c superconductor LSCO. The system parameters for LSCO are given in Table I. All parameters are given in atomic units. With these choices energy is measured in Hartrees, E_H , with $1E_H \approx 27.2$ eV, length is measured in Bohr radii, $a_B \approx 0.53 \text{ \AA}$, $\hbar = 1$ and electron mass $m = 1$. The temperature of the system, T_0 , is 16.3 K and the maximum energy ϵ_{\max} from Eq. (B1) is $0.000356E_H$. The Fermi distribution of the thermal reservoirs at this temperature is shown in Fig. 3. The choice of temperature is such that one propagating mode exists in the device. We will generally bias the leftmost normal lead and we will be setting $v_l = 0.1\Delta_0$ for all of our numerical results. Unless explicitly stated otherwise, the numerical results will be for $L_S = 6\xi$ and $L_N^C = 2.75\xi$, where ξ is the superconducting coherence length.

In this paper we restrict ourselves to the quasi-1D limit and as such only consider the first propagating channel of the waveguide [1,14]. The transverse dimensions of the system, L_x and L_y , are set such that, for the given ϵ_{\max} and T_0 we have selected, all of the transport through the system is restricted to just the first propagating channel. The system size is small enough and temperature low enough that electron transport in the quasi-one-dimensional wire is assumed to be ballistic. We also assume that a phase difference of ϕ can be induced between the superconducting segments, although this is not essential for our main results.

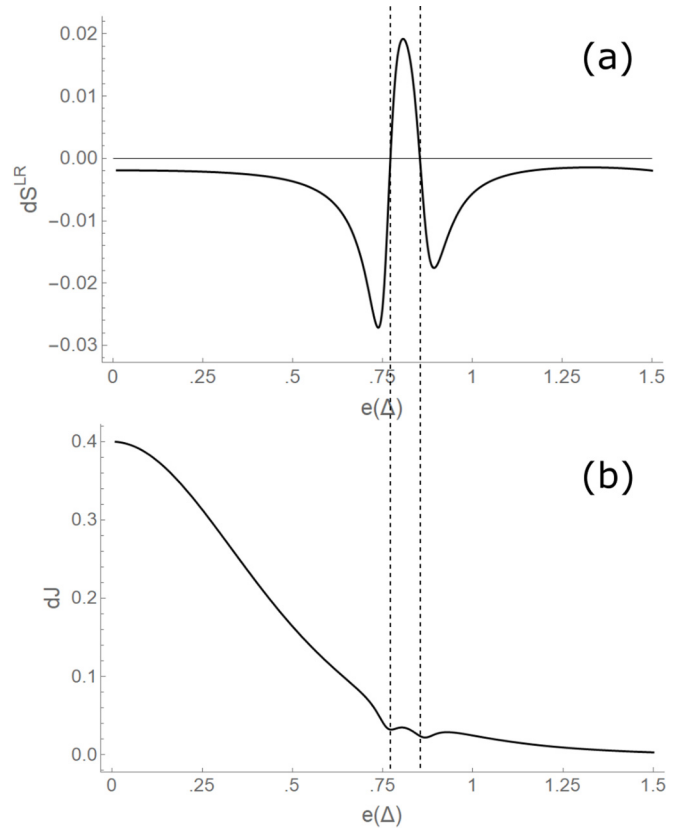


FIG. 4. Energy distribution for the (a) cross-correlated shot noise and (b) current with $L_S = 6\xi$, $L_N^C = 2.75\xi$ and $\phi = 0$. Lines have been drawn on the current plot to highlight the overlap between the current distribution and the positive region of the cross-correlated shot noise.

V. CROSS-CORRELATED SHOT NOISE FOR NSNSN

Figure 4 shows plots of the shot noise distribution $dS^{LR}(e)$ and average current $dJ(e)$ as a function of energy for $L_S = 6\xi$ and $L_N^C = 2.75\xi$. We can see that there is a subgap energy interval where the cross-correlated shot noise is positive. In Fig. 4(b) we plot the energy distribution of the current. Vertical lines have been drawn in to highlight the overlap between these distributions in the region of positive cross-correlated shot noise. We can see that a nontrivial fraction of the current is indeed carried by electrons in this energy interval.

The size of the superconducting regions affects the behavior of the cross-correlated shot noise. In Figs. 5(a) and 5(b) we plot the cross-correlated noise energy distributions for superconducting regions ranging in length from $L_S = 1\xi$ to $L_S = 9\xi$ with L_N^C fixed at 2.75ξ . For small values of L_S ($1\xi \leq L_S \leq 4\xi$) [shown in Fig. 5(a)] we see no energy intervals of positive cross-correlated shot noise. For larger values of L_S , ($4\xi \leq L_S \leq 9\xi$) shown in Fig. 5(b), we do see energy intervals with positive cross-correlated shot noise. The maximum values of the positive peak decreases as we increase L_S beyond $L_S = 6\xi$. At intermediate values of L_S ($4\xi \leq L_S \leq 6\xi$), we find large positive peaks in the positive cross-correlated shot noise with finite energy width. In Sec. IX we will evaluate the relationship between the positive cross-correlated noise and the size of L_S and L_N^C in more detail.

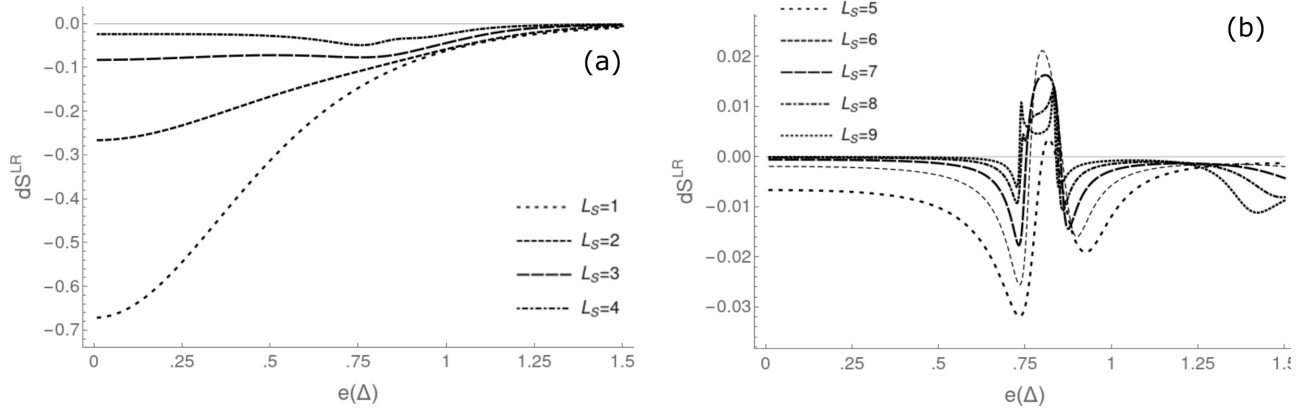


FIG. 5. Differential cross-correlated shot noise for a number of different superconducting region sizes. In (a) $L_S = 1 - 4$ and in (b) $L_S = 5 - 9$, in units of the coherence length. For both (a) and (b) the size of the central normal region is 2.75ξ .

VI. SCATTERING AMPLITUDES FOR NSNSN

In Fig. 6 we give plots of $|t_{pp}^{LR}|$, $|t_{hh}^{LR}|$ and $|t_{ph}^{LR}|$ for a few different values of L_S and ϕ . For Figs. 6(a)–6(c) $L_S = 6\xi$ and $L_N^C = 2.75\xi$. The phase differences between the two superconducting regions, in Figs. 6(a)–6(c), ϕ , are 0 , $\frac{\pi}{6}$, and $-\frac{\pi}{6}$, respectively. In Fig. 6(d), $L_S = 8\xi$, $L_N^C = 2.75\xi$, and $\phi = \frac{\pi}{6}$.

In Fig. 6(a), there is a pair of resonances in the transmission amplitudes with peaks in t_{pp}^{RL} , t_{hh}^{RL} , and t_{hp}^{RL} below the gap

energy. There is a small shift in the peaks of the particle-particle and hole-hole resonances due to the small momentum difference between particles and holes with the same energy. There is also a resonance in t_{hp}^{RL} . As we change the phase difference ϕ , the offset in the positions of the t_{pp}^{RL} and t_{hh}^{RL} resonances increases, with the positions of the peaks for t_{pp}^{RL} and t_{hh}^{RL} dependent on the sign of the phase difference. At the same time, as we increase ϕ the magnitude of the second resonance in t_{pp}^{RL} and t_{hh}^{RL} markedly decreases.

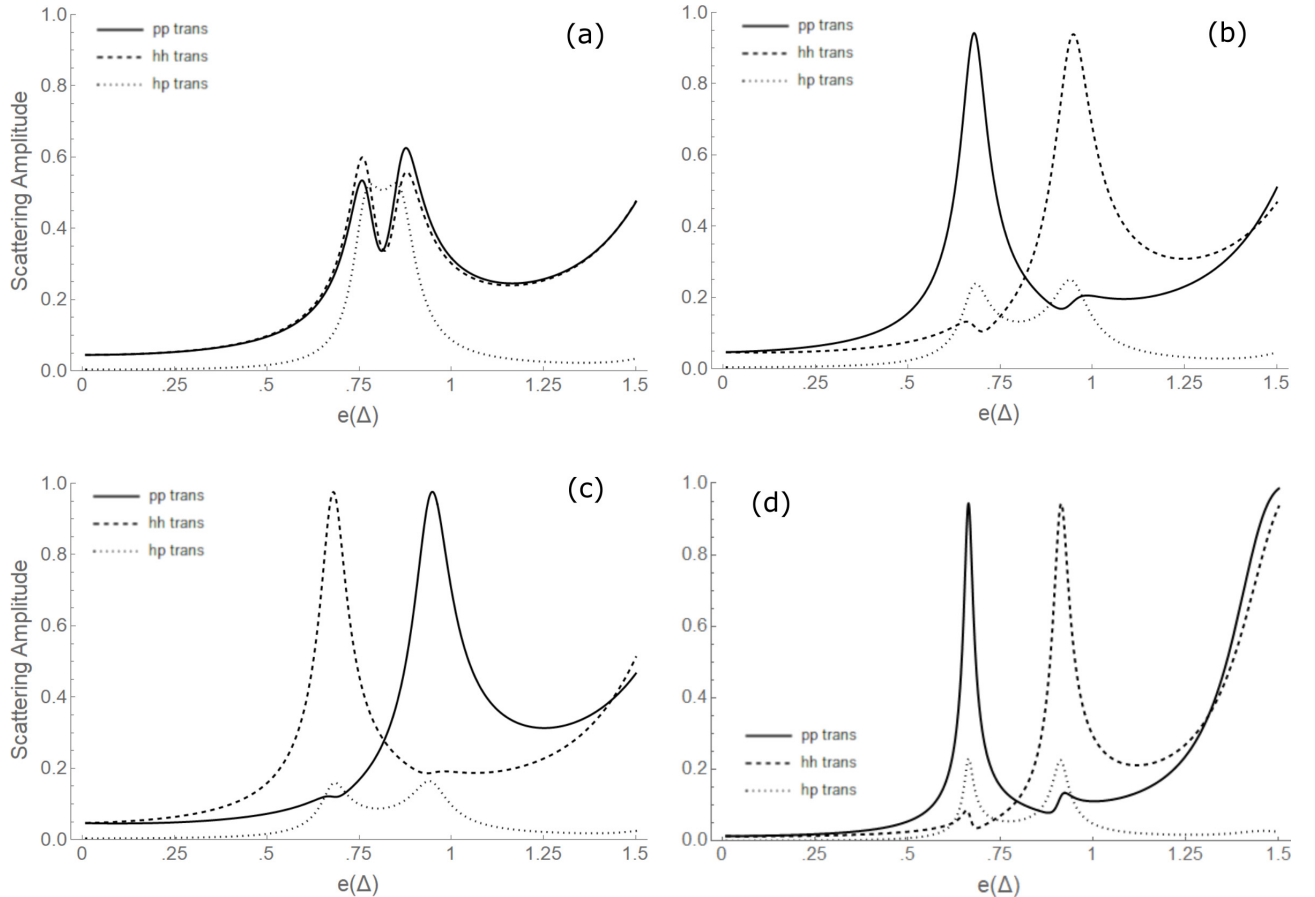


FIG. 6. Plots of the magnitudes of the particle-particle, hole-hole, and particle-hole transmission coefficients for a variety of system parameters. (a) $L_S = 6\xi$ and $\phi = 0$, (b) $L_S = 6\xi$ and $\phi = \frac{\pi}{6}$, (c) $L_S = 6\xi$ and $\phi = -\frac{\pi}{6}$, (d) $L_S = 8\xi$ and $\phi = \frac{\pi}{6}$.

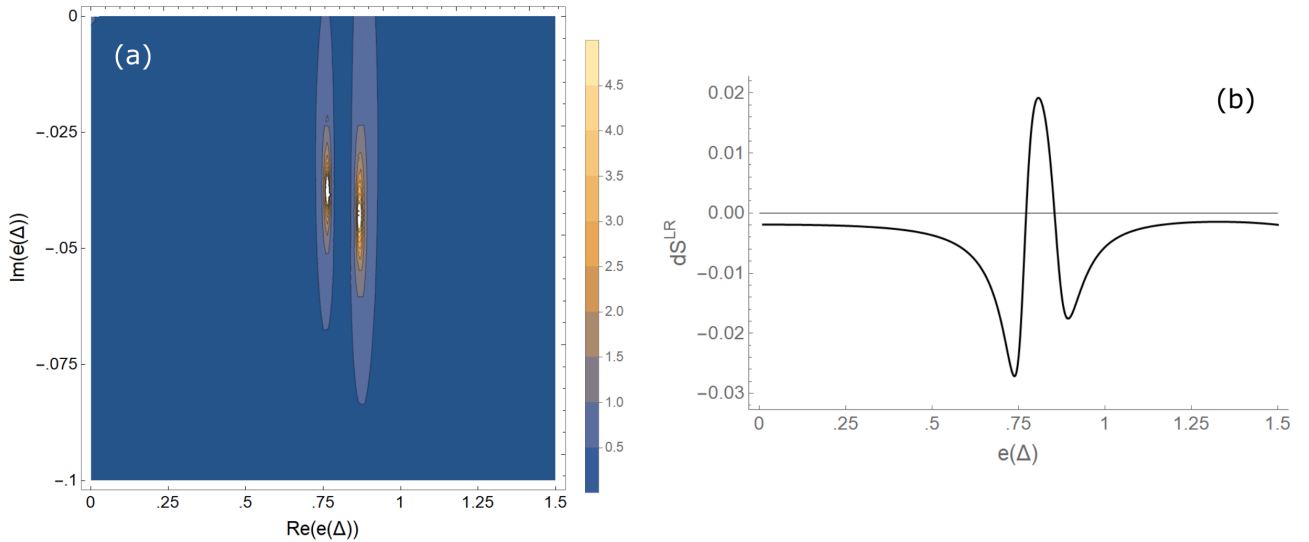


FIG. 7. (a) Plot of the $|t_{pp}^{LR}|$ in the complex energy plane for $L_S = 6\xi$ and $L_C^N = 2.75\xi$. The poles correspond to the quasibound state resonances in Fig. 6(a). (b) Corresponding plot of $dS^{LR}(e)$.

In Fig. 6(d) we see that increasing the size of the superconducting regions results in sharper resonances. Whereas it appears in Figs. 6(a)–6(c) that t_{ph}^{RL} has a centrally located resonance in-between the t_{pp}^{RL} and t_{hh}^{RL} resonances, t_{ph}^{RL} actually has a pair of resonances at the same energies as the t_{pp}^{RL} and t_{hh}^{RL} resonances. A key feature we see in the scattering plots is that for $L_S = 6\xi$ at small values of ϕ there is a small energy interval in-between the resonances in t_{pp}^{RL} and t_{hh}^{RL} , where t_{ph}^{RL} becomes the dominant transmission term. This energy interval corresponds nearly exactly to the energy interval in which we observed a positive peak for $dS^{LR}(e)$ in Fig. 4(a).

VII. QUASIBOUND STATES AND POLE STRUCTURE

We saw in Fig. 6 clear evidence for the existence of resonances in the plots of t_{pp}^{RL} , t_{hh}^{RL} , and t_{hp}^{RL} . Below the gap, excitations in the central normal region are confined by

repeated Andreev reflections at each of the interfaces. In the NSNSN geometry, this produces quasibound states, as the finite size of the superconducting regions allow particles and holes to tunnel out at a nonzero rate.

In Fig. 7(a) we plot $|t_{pp}^{RL}|$ for complex energy values and for the same parameters used in Fig. 6(a). The contour plot in Fig. 7 shows that the resonances in t_{pp}^{RL} in Fig. 6(a) is actually due to a pair of closely spaced poles in the complex energy plane.

In Fig. 7(b) we have the corresponding plot of $dS^{LR}(e)$. Away from the quasibound states $dS^{LR}(e)$ is entirely negative. At the quasibound state energy, however, there is a large positive peak in the value of $dS^{LR}(e)$. This connection between the positivity of $dS^{LR}(e)$ and the positions of the quasibound states is fairly general as well. In Fig. 8 we plot the complex poles and the cross-correlated noise for a longer central normal region, $L_S = 6\xi$ and $L_C^N = 5\xi$. Increasing L_C^N

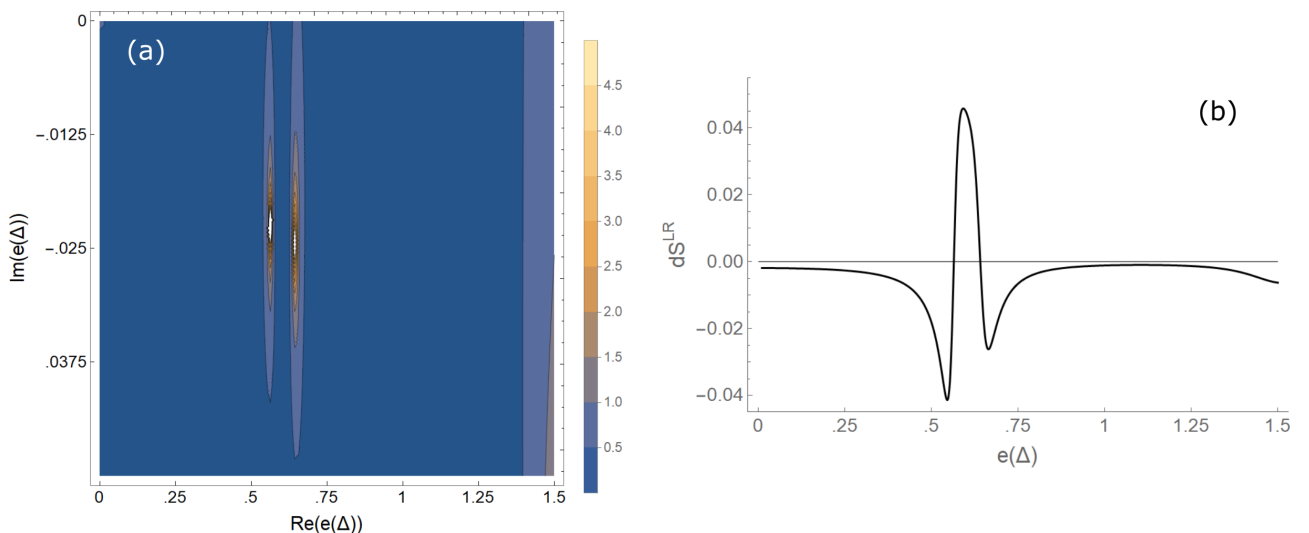


FIG. 8. (a) Magnitude of $|t_{pp}^{LR}|$ in the complex energy plane for $L_S = 6\xi$ and $L_C^N = 5\xi$. (b) Corresponding plot of $dS^{LR}(e)$.

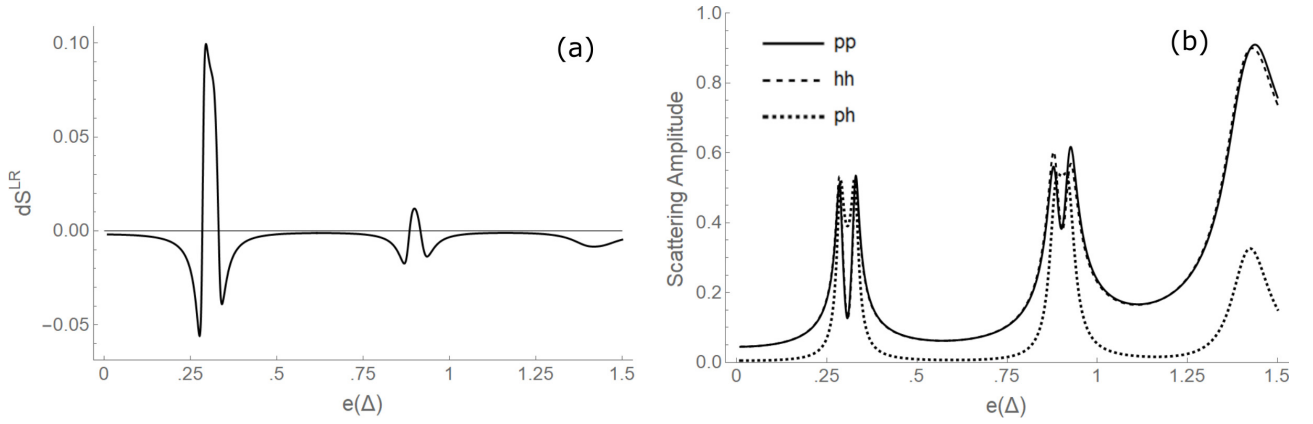


FIG. 9. (a) Plot of $dS^{LR}(e)$ for $L_S = 6\xi$ and $L_N^C = 13\xi$. Note the existence of multiple positive peaks in the energy distribution. (b) Corresponding plots of $|t_{pp}^{LR}|$, $|t_{hh}^{RL}|$, and $|t_{hp}^{RL}|$. There is a one-to-one correspondence between the resonances and the positive noise correlations.

has the effect of decreasing the real and imaginary parts of the quasibound state energies. In Fig. 8(b) the energy interval with positive cross-correlated shot noise has shifted to the left in accordance with the movement of the quasibound states.

For sufficiently large values of L_N^C we can start to have additional quasibound states emerge, which results in additional scattering resonances and additional positive peaks in the plots of $dS^{LR}(e)$. This can be seen in Fig. 9, where we plot $dS^{LR}(e)$ and the transmission coefficients for $L_S = 6\xi$ and $L_N^C = 13\xi$.

In addition to modifying the quasibound state energies by changing L_N^C , we can also change ϕ . In Fig. 10 we plot the poles of t_{pp}^{LR} with (a) $\phi = \frac{\pi}{12}$ and (b) $\phi = -\frac{\pi}{12}$. Increasing the phase difference in the positive direction shifts the real energy of the pole on the left and shrinks the size of the pole on the right. With a negative phase difference it is now the pole on the left that shifts its real energy and shrinks. However, while it is possible to shift the positions of the quasibound states by adjusting the value of ϕ , this can have the effect of reducing the positivity of the noise correlations. This is seen in Fig. 11, where $dS^{LR}(e)$ is plotted as a function of both the energy, e , and the phase difference ϕ . Positive values of $dS^{LR}(e)$ are localized about a small range of ϕ values near zero. This

suggests that for the goal of maximizing the positivity of $dS^{LR}(e)$ it is best to set $\phi = 0$.

VIII. ORIGIN OF POSITIVE NOISE CROSS-CORRELATION

In the previous section, we observed a connection between the location of the quasibound state poles and the energy intervals of positive cross-correlated shot noise. In this section, we show the origin of the positive contributions to the cross-correlated shot noise at the resonance energies.

In Fig. 12, we plot the three terms, dS_{pp}^{LR} , dS_{hh}^{LR} , and dS_{ph}^{LR} separately. Away from the resonances the only term which goes positive is dS_{ph}^{LR} . However, at the resonance we see that dS_{pp}^{LR} , dS_{hh}^{LR} , and dS_{ph}^{LR} switch behaviors and now there is an overall negative contribution due to dS_{ph}^{LR} and an overall positive contribution due to dS_{pp}^{LR} and dS_{hh}^{LR} . Since dS_{pp}^{LR} and dS_{hh}^{LR} have similar qualitative behavior we will focus on just the positive contributions arising from dS_{pp}^{LR} .

The contribution to the shot noise from dS_{pp}^{LR} is given in Eq. (7). It can be split into three terms, each with a different dependence on the thermal reservoirs. They are

$$dS_{pp}^{LR}(1) = \frac{m_L m_R}{\pi^2 \hbar^4} F_p^L N_p^L ((-|r_{hp}^{LL}|^2 + |r_{pp}^{LL}|^2 - 1) (-|t_{hp}^{RL}|^2 + |t_{pp}^{RL}|^2)), \quad (10)$$

$$dS_{pp}^{LR}(2) = \frac{m_L m_R}{\pi^2 \hbar^4} F_p^R N_p^R ((-|r_{hp}^{RR}|^2 + |r_{pp}^{RR}|^2 - 1) (-|t_{hp}^{LR}|^2 + |t_{pp}^{LR}|^2)), \quad (11)$$

$$dS_{pp}^{LR}(3) = \frac{m_L m_R}{\pi^2 \hbar^4} (F_p^L N_p^R + F_p^R N_p^L) (\text{Re}[r_{hp}^{LL} r_{hp}^{RR} t_{hp}^{LR*} t_{hp}^{RL*}] - \text{Re}[r_{hp}^{LL*} r_{pp}^{RR*} t_{pp}^{RL} t_{hp}^{LR}] + \text{Re}[r_{pp}^{LL} r_{pp}^{RR} t_{pp}^{LR*} t_{pp}^{RL*}] - \text{Re}[r_{pp}^{LL*} r_{hp}^{RR*} t_{hp}^{RL} t_{pp}^{LR}]). \quad (12)$$

In Figs. 13(a)–13(c) we plot each of these three terms separately.

We now focus on $dS_{pp}^{LR}(1)$. Expanded out fully $dS_{pp}^{LR}(1)$ has six separate components, three of which give rise to positive correlations at the resonance. These three terms, are (neglecting the Fermi distribution prefactors) $\Sigma_1 = |t_{pp}^{RL}|^2 |r_{pp}^{LL}|^2$, $\Sigma_2 = |t_{hp}^{RL}|^2$ and $\Sigma_3 = |r_{hp}^{RL}|^2 |r_{hp}^{LL}|^2$. In Fig. 13(d)–13(f) we give their respective plots. The largest of the three contributions is due to

the Σ_2 term, which corresponds to the CAR process [11]. The remaining two terms are characterized using a scheme based on [14] and [39]. Each of the higher-order products of scattering coefficients consists of two reflection coefficients, either normal reflection (NR) (r_{pp} or r_{hh}) or Andreev reflection (AR) (r_{ph} and r_{hp}), and two transmission coefficients, either elastic cotunneling (EC) (t_{pp} or t_{hh}) or crossed Andreev reflection (CAR) (t_{ph} or t_{hp}). Using this scheme Σ_1 is called an EC-NR

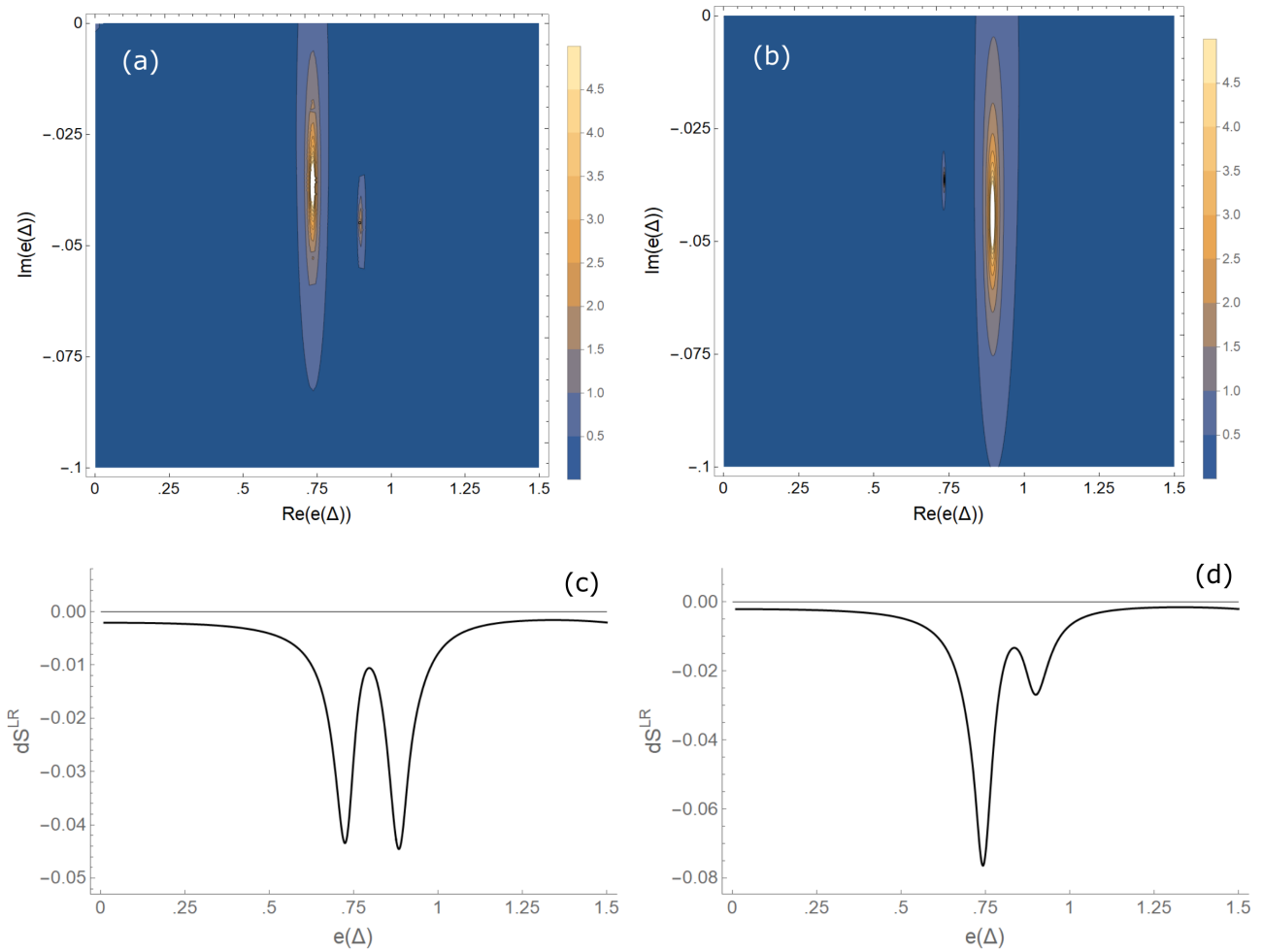


FIG. 10. Poles of $|t_{pp}^{LR}|$ for (a) $\phi = \frac{\pi}{12}$ and (b) $\phi = -\frac{\pi}{12}$, with the corresponding plots of $dS^{LR}(e)$ given in (c) and (d) respectively. As we change the phase difference the second resonance we saw in Fig. 7 becomes smaller and eventually disappears entirely.

term, as it consists of two normal transmission and two normal reflection coefficients, and Σ_3 is called a CAR-AR term, as it

consists of two Andreev reflection and two crossed Andreev reflection coefficients.

In contrast to [14,39], which found that at $T = 0$ EC-NR and CAR-AR terms always results in negative correlations,

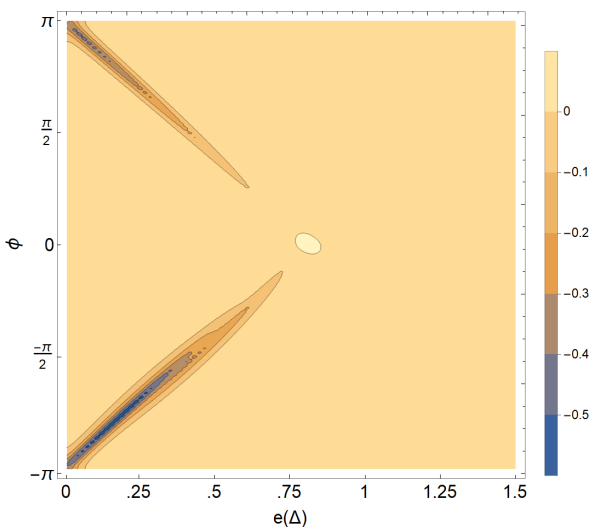


FIG. 11. Phase dependence of the cross-correlated shot noise. We can see that there region of positive shot noise is localized around the value $\phi = 0$, and is maximized at that point in general.

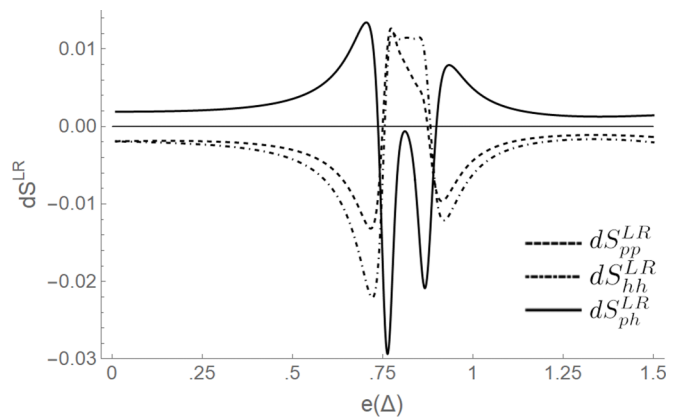


FIG. 12. Contributions to the differential cross-correlated shot noise dS_{pp}^{LR} , dS_{hh}^{LR} , and dS_{ph}^{LR} (plotted separately), for $L_S = 6\xi$ and $L_N^C = 2.75\xi$. Away from resonance dS_{pp}^{LR} and dS_{hh}^{LR} are negative and dS_{ph}^{LR} is positive. At resonance dS_{pp}^{LR} and dS_{hh}^{LR} are positive and dS_{ph}^{LR} is negative.

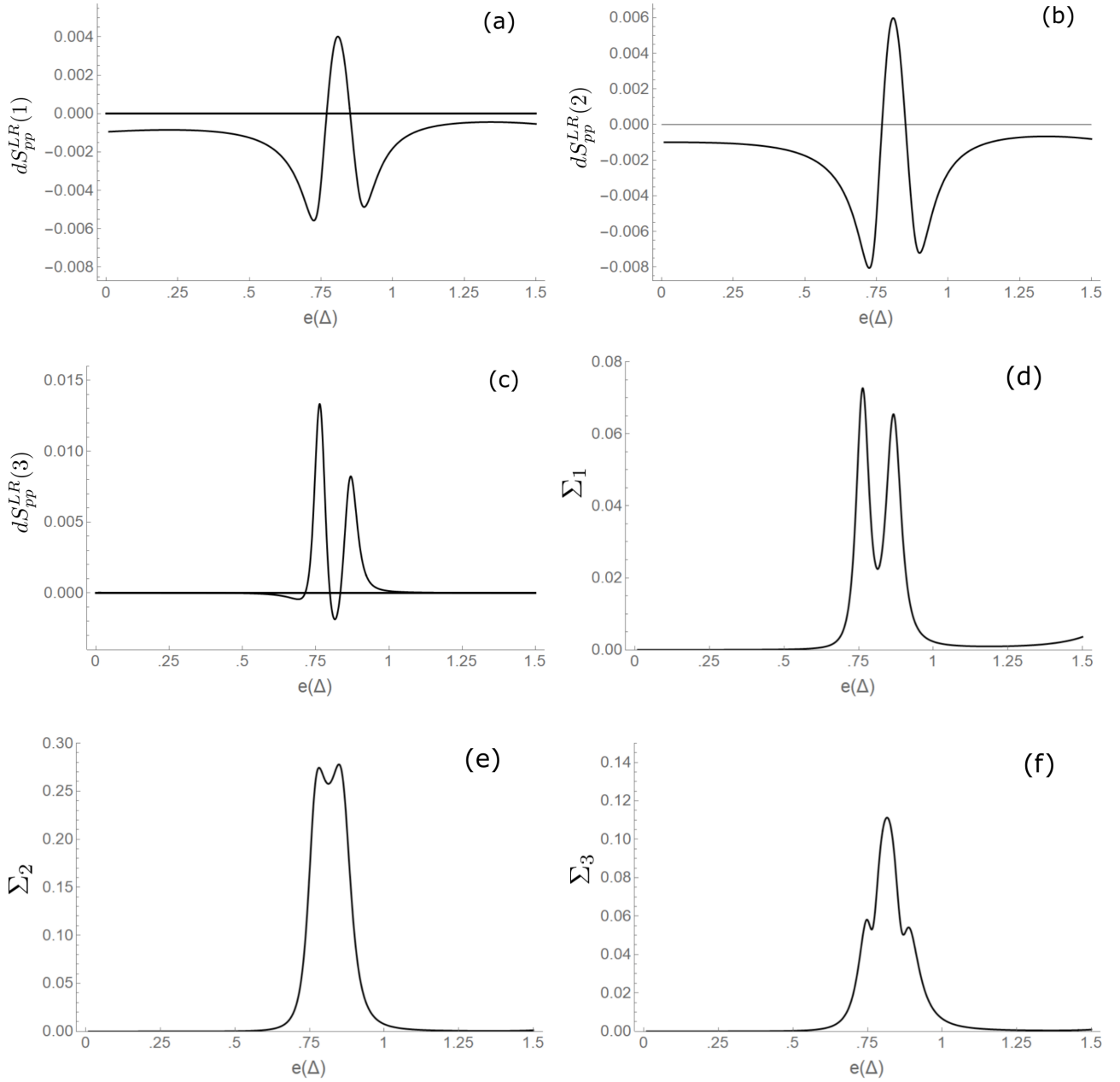


FIG. 13. Plots of components of dS_{pp}^{LR} for $L_S = 6\xi$ and $L_N^C = 2.75\xi$. (a) $dS_{pp}^{LR}(1)$. (b) $dS_{pp}^{LR}(2)$. (c) $dS_{pp}^{LR}(3)$. All three components are negative away from the resonance but contribute positively at the resonance energies. Additionally, plots of the three components of S_{pp}^{LR} , (d) $\Sigma_1 = |t_{pp}^{RL}|^2 |r_{pp}^{LL}|^2$, (e) $\Sigma_2 = |t_{hp}^{RL}|^2$, (f) $\Sigma_3 = |t_{hp}^{RL}|^2 |r_{hp}^{LL}|^2$.

at finite temperatures in the NSNSN system these terms can indeed give positive contributions, as seen in Figs. 13(d) and 13(f). The EC-NR term arises microscopically due to correlations induced by the elastic cotunneling scattering processes [14]. The CAR-AR term arises microscopically from a process referred to as synchronized Andreev reflection (AR-AR), a higher-order process in which a pair of Andreev reflections (from particle to hole or vice versa) at the leftmost and rightmost interfaces occur in a coherent fashion [40].

IX. SYSTEM SIZE DEPENDENCE AND COMPARISON TO NSN GEOMETRY

It is important to compare results for the NSNSN system with those of the simpler NSN geometry. In particular, we

are interested in comparing results in the case where the size of the central superconducting region S in the NSN geometry is the same size as the central SNS structure in the NSNSN geometry. In Fig. 14(a) we plot the cross-correlated noise distributions for an NSNSN system with $L_S = 6\xi$ and $L_N^C = 2.75\xi$ and an NSN system with $L_S = 14.75\xi$. Unlike the NSNSN system, for the NSN system we no longer see any energy intervals in which dS^{LR} goes positive. This is not just the case for this choice of system size either. In Fig. 14(b) we plot dS^{LR} for a range of superconducting region sizes for the NSN system ranging from $L_S^{NSN} = 1.75\xi$ to $L_S^{NSN} = 14.75\xi$, and for all of these system sizes we see that the total cross-correlated noise distribution remains negative over the full energy range of the system.

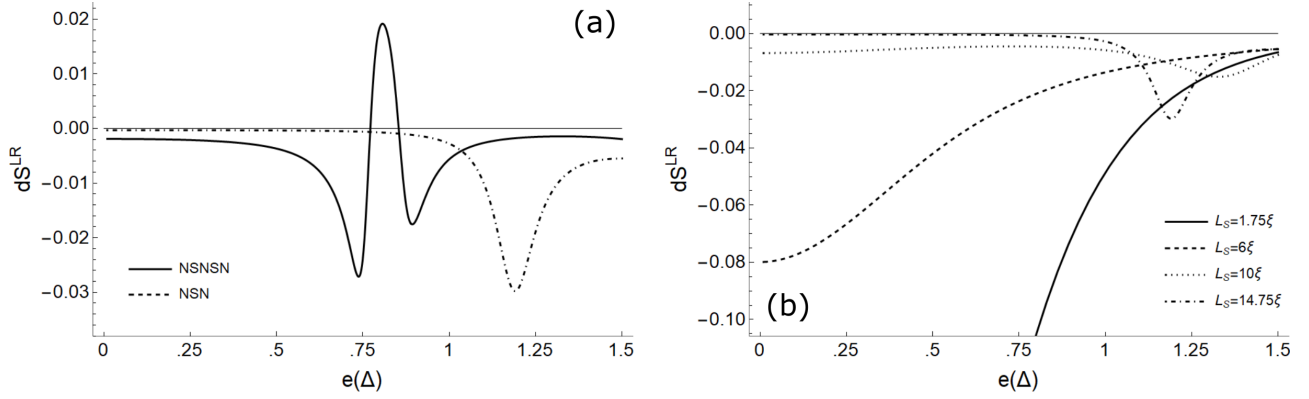


FIG. 14. (a) Comparison $dS^{LR}(e)$ for the NSNSN and NSN geometries. For the NSNSN system $L_S = 6\xi$ and $L_N^C = 2.75\xi$ and for the NSN system $L_S^{NSN} = 14.75\xi$. (b) Plot of dS^{LR} for the NSN system with $L_S^{NSN} = 1.75\xi, 6\xi, 10\xi$ and 14.75ξ . The total cross-correlated noise energy distribution remains negative over the entire energy interval.

We will now readdress the relationship between the system size and the positivity of dS^{LR} discussed in Sec. V (specifically in Fig. 5). To do so we will define the quantity

$$S_+^{LR} = \int de \text{clip}_+(dS^{LR}(e)), \quad (13)$$

where

$$\text{clip}_+(x) = \begin{cases} 0 & x < 0 \\ x & x \geq 0. \end{cases} \quad (14)$$

This expression corresponds to the total area of the positive regions of dS^{LR} and gives us a simple measure with which to compare the positivity of the cross-correlated noise for different values of L_S and L_N^C . In Fig. 15 we have a contour plot of S_+^{LR} as a function L_S and L_N^C . One feature we immediately recover, which we saw indications of in Fig. 5 is the existence of a “sweet spot” for the value of L_S which maximizes S_+^{LR} . This behavior of the NSNSN system, namely, zero positivity

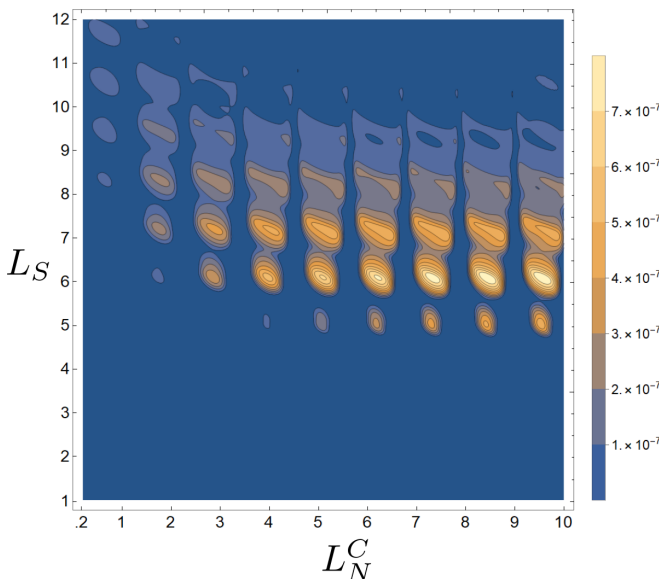


FIG. 15. Area of the region of positive noise correlations S_+^{LR} , as a function of the system size, with values of L_S along the y axis and values of L_N^C along the x axis.

in the noise cross-correlations for both very small and large values of L_S , appears to be a general feature of the NSNSN geometry. Also, Fig. 15 shows a periodic-like relationship between S_+^{LR} and L_N^C , in which a series of peaks in S_+^{LR} is separated by troughs where S_+^{LR} is nearly zero. As we increase L_N^C the maximum value of S_+^{LR} increases accordingly. An interesting question for future analysis is whether the maximum values of S_+^{LR} continue to grow monotonically as we increase L_N^C further.

X. TEMPERATURE DEPENDENCE

In Sec. IV we explained that the choice of temperature $T_0 = 16.3$ K was based on ensuring that the transport was effectively restricted to the first transverse mode of the system (so as to simplify our calculations) balanced with the requirement that there was a nontrivial population of excitations throughout the full energy range comprising the first transverse mode of the system. The balancing of these two requirements can be seen in the Fermi distribution of the leftmost lead plotted in Fig. 3. It is interesting to consider the cross-correlated noise of the system as we lower the temperature of the system.

In Fig. 16(a) we show a plot of the cross-correlated shot noise as a function of both energy and system temperature, T_0 , for temperatures ranging from 0 K to 16.3 K, and for $L_N^C = 2.75\xi$, $L_S = 6\xi$, and $v_l = .1\Delta_0$. From Fig. 16(a) we can see that the behavior of the cross-correlated noise energy distribution as a function of temperature breaks into roughly three regimes. At close to $T_0 = 16.3$ K the distribution is heavily dependent on the quasibound state located roughly halfway through the energy range of the system. At intermediate temperatures the population of excitations at energies near the quasibound state is suppressed and, while we still see a positive peak at the quasibound state as seen in Fig. 16(b) for $T_0 = 8.15$ K, the magnitude of that peak is nearly twenty times smaller than what was seen in Fig. 7(b).

Finally, at very low temperatures we see a new behavior in which we have a positive peak in the shot noise distribution at energies just below the bias energy $v_l = 0.1\Delta_0$. This behavior is demonstrated in Fig. 16(c), where we have set $T_0 = 1$ K. This peak is not associated with any quasibound states of the

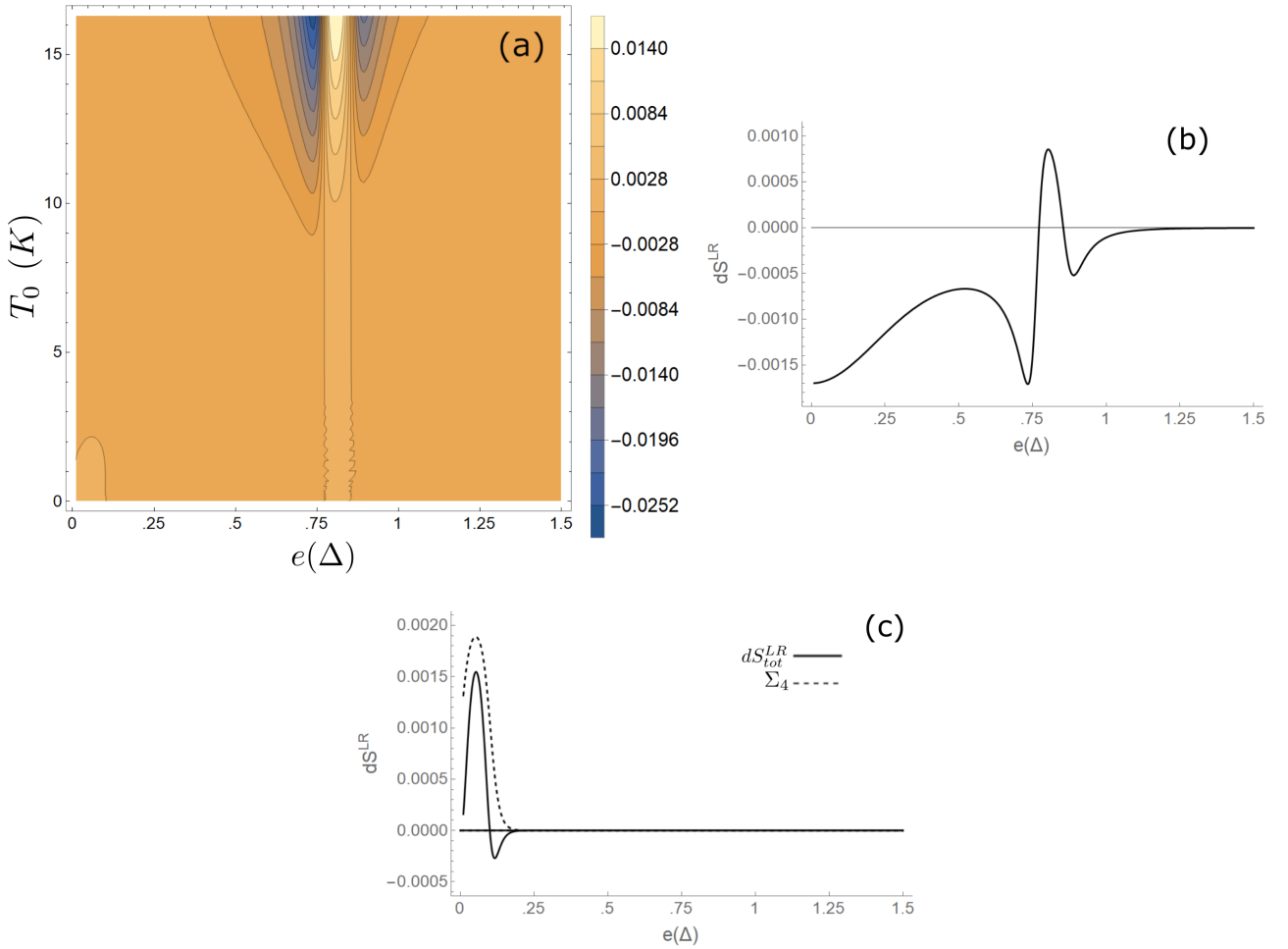


FIG. 16. (a) Plot of the cross-correlated shot noise distribution as a function of the system temperature, T_0 , and energy e with $L_N^C = 2.75\xi$ and $L_S = 6\xi$. (b) Cross-correlated shot noise distribution for $T_0 = 8.15$ K. (c) Cross-correlated shot noise distribution for $T_0 = 1$ K plotted alongside the subterm $\Sigma_4 = -(F_h^L N_p^R + F_p^R N_h^L) \text{Re}[r_{ph}^{LL*} r_{ph}^{RR*} t_{pp}^{LR} t_{hh}^{RL}]$, which is the primary positive contribution.

system and can be traced back to a specific subcomponent of dS_{ph}^{LR} , $\Sigma_4 = -(F_h^L N_p^R + F_p^R N_h^L) \text{Re}[r_{ph}^{LL*} r_{ph}^{RR*} t_{pp}^{LR} t_{hh}^{RL}]$, which is plotted alongside the total cross-correlated noise distribution in Fig. 16(c). Using the classification scheme discussed in Sec. VIII the term $-(F_h^L N_p^R + F_p^R N_h^L) \text{Re}[r_{ph}^{LL*} r_{ph}^{RR*} t_{pp}^{LR} t_{hh}^{RL}]$ corresponds to an EC-AR term. It was shown in Ref. [14,39] that EC-AR terms in the cross-correlated noise correspond microscopically to a process called synchronized Andreev and inverse Andreev reflection (AR-AR), a higher-order process in which an Andreev reflection (from particle to hole) at one interface and an inverse Andreev reflection (from hole to particle) at the other interface occur in a coherent fashion. Due to the simultaneous exchange of two fermions, the correlations resulting from this process can be boson-like, and as such positive.

XI. THE ANDREEV APPROXIMATION

We have so far presented results of the full scattering theory and thus far have not looked at the effect of applying the Andreev approximation [37]. The Andreev approximation can be used if the ratio between the gap energy Δ_0 and the Fermi energy E_F , $\frac{\Delta_0}{E_F}$, is sufficiently small. Then to good

approximation we can drop higher order terms in the ratio $\frac{\Delta_0}{E_F}$ from the BdG equations. Doing so reduces the pair of coupled second order differential equations in Eq. (A1) to a pair of coupled first-order differential equations known as the Andreev equations.

Under the Andreev approximation the quasiparticle dynamics of the system are governed by a pair of coupled first order differential equations, and the boundary conditions connecting the different regions reduces to just the continuity of the wave functions at the boundary. In the high-transparency limit we consider here, this gives $r_{pp}^{LL} = r_{hh}^{LL} = r_{pp}^{RR} = r_{hh}^{RR} = 0$ as well as $t_{hp}^{LR} = t_{ph}^{LR} = t_{hp}^{RL} = t_{ph}^{RL} = 0$ in the scattering matrix (with the remaining scattering elements modified accordingly). Note that this approach, starting from the Andreev equations and then solving for the scattering matrix using just the continuity of the wave functions at the interface, appears to be different than the approach described in the original BTK paper [35], which starts from the full scattering matrix of the system and takes the limit $q_p^\alpha = q_h^\alpha = k_p^\alpha = k_h^\alpha = k_F$, where $\alpha \in \{L, C, R\}$. We have found, by direct calculation, that using the BTK approach gives results exactly identical to those found using the Andreev equations directly. Perhaps the key advantage of applying the Andreev approximation is

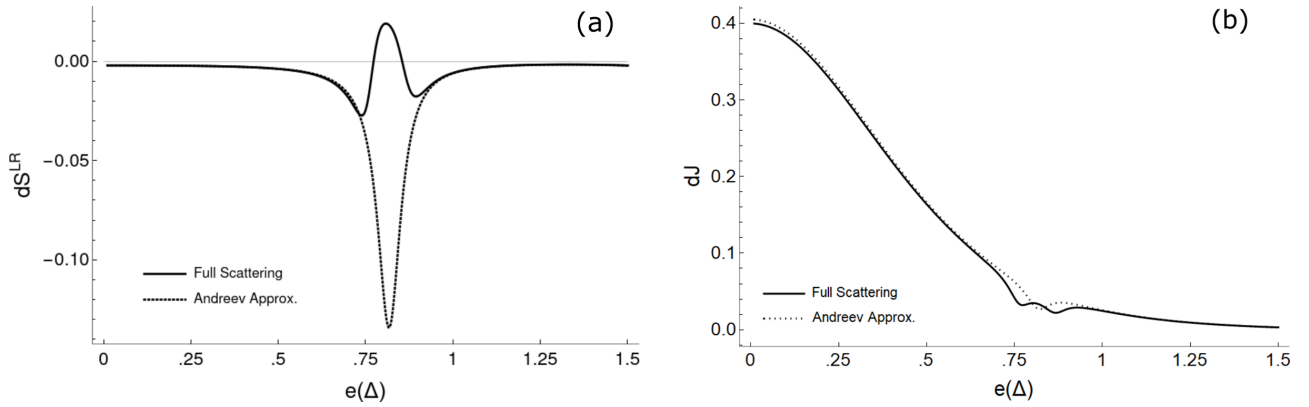


FIG. 17. Comparison between the full scattering theory and results using the Andreev approximation. In (a) the differential cross-correlated shot noise and in (b) the magnitude of the current. While the results agree well away from the resonance, at the resonance we see that the Andreev approximation breaks down badly for the noise.

that it vastly simplifies the resulting expressions for the scattering coefficients and noise. With the Andreev approximation applied it is possible to write down the explicit expressions for the scattering elements, and they are given in Appendix C along with the simplified cross-correlated shot noise.

In Fig. 17 we compare the cross-correlated shot noise and current distributions from the full scattering theory and using the Andreev approximation. Away from the resonance the results using the Andreev approximation are nearly indistinguishable qualitatively from the full scattering theory. At energies close to the resonance, however, we see from Fig. 17(a) that the behavior of $dS^{LR}(e)$ strongly diverges. Whereas there is a clear positive peak in the noise distribution in the full scattering theory results, using the Andreev approximation the noise distribution remains purely negative and instead has a large negative dip at the resonance. The choice to use LSCO's parameters in our model system was motivated partly by it having one of the largest values of $\frac{\Delta_0}{E_F}$ among commonly studied superconductors, so it is an ideal substance for analyzing the Andreev approximation. The key issue here is the fact that the Andreev approximation treats terms such as $|r_{ph}^{LR}|$ and $|r_{pp}^{LL}|$ as negligible, while in reality these terms are nontrivial for the NSNSN system and are components of the main positive contributions to the cross-correlated noise, as seen in Fig. 13.

There are also some qualitative differences to be found in the results for the quasibound states of the system. In Fig. 18 we plot the poles of $|r_{pp}^{LR}|$ using the Andreev approximation. While the energy of this pole is comparable to what was found using the full scattering scattering theory in Fig. 7(a), we now find only a single pole as opposed to the pair of poles.

XII. CONCLUSIONS

In previous sections, we studied the scattering properties and the current and cross-correlated shot noise distributions of an NSNSN system. We have obtained analytical expressions for the scattering matrix of the system without the Andreev approximation. We then used the scattering matrix elements to calculate the current and cross-correlated shot noise energy distributions and have used numerics to plot these quantities

for a variety of system parameters. We find a one-to-one correspondence between the energies of quasibound states in the system and regions of positive correlations in the cross-correlated shot noise distributions. This connection between the positions of the quasibound states and the positive noise correlations is robust and is shown to be the case even as we introduce multiple quasibound states by increasing our system size. Moreover, we find that while the Andreev approximation gives strong qualitative agreement for the current and cross-correlated shot noise at energies away from the quasibound states, it breaks down notably at the quasibound state energies. We also find differences between the results of the full scattering theory and the Andreev approximation when looking at the poles of the scattering matrix in the complex energy plane.

ACKNOWLEDGMENTS

The authors thank the Robert A. Welch Foundation (Grant No. F-1051) for support of this work.

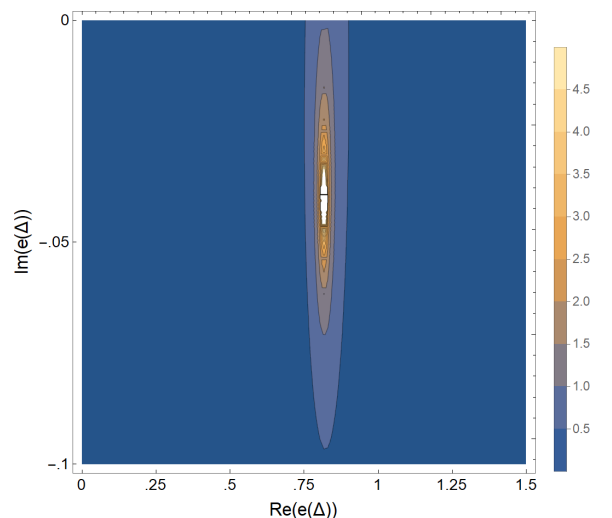


FIG. 18. Quasibound state pole using the Andreev approximation. While at approximately the same energy, we do not see the double poles we did in Figs. 7 and 8.

APPENDIX A: BOGOLIUBOV-DE GENNES EQUATIONS AND SCATTERING THEORY

We use the Bogoliubov-de Gennes formalism [33] for superconductivity to derive the scattering matrix for the NSNSN system. Within the superconductor, the energy eigenstates in real-space are given by solutions to the Bogoliubov-de Gennes equations,

$$\begin{pmatrix} -\frac{\hbar^2 \nabla^2}{2m} - E_F & \Delta(\mathbf{r}) \\ \Delta^*(\mathbf{r}) & \frac{\hbar^2 \nabla^2}{2m} + E_F \end{pmatrix} \begin{pmatrix} u(\mathbf{r}) \\ v(\mathbf{r}) \end{pmatrix} = e \begin{pmatrix} u(\mathbf{r}) \\ v(\mathbf{r}) \end{pmatrix}, \quad (\text{A1})$$

where E_F is the Fermi energy, $\Delta(\mathbf{r})$ is the spatially varying gap function, e is the quasiparticle eigenenergy, m is the effective electron mass, and $u(\mathbf{r})$ and $v(\mathbf{r})$ are the coherence factors and satisfy the condition $\int d\mathbf{r} (|u(\mathbf{r})|^2 + |v(\mathbf{r})|^2) = 1$. With reference to the points labeled in Fig. 1, the gap function is given by

$$\Delta(\mathbf{r}) = \begin{cases} 0 & z < 0, \quad h_1 < z < h_2, \quad h_3 < z \\ \Delta_0 & 0 \leq z \leq h_1 \\ \Delta_0 e^{i\phi} & h_2 \leq z \leq h_3. \end{cases} \quad (\text{A2})$$

The coherence factors u_0 and v_0 , and the wave vectors k_p and k_h [see Eq. (1)] are given by

$$u_0 = \sqrt{\frac{1}{2} \left(1 + \frac{\sqrt{e^2 - \Delta_0^2}}{e} \right)} \quad v_0 = e^{i\phi} \sqrt{\frac{1}{2} \left(1 - \frac{\sqrt{e^2 - \Delta_0^2}}{e} \right)} \quad k_p = k_F^S \sqrt{1 + \frac{e^2 - \Delta_0^2}{(E_F^S)^2}} \quad k_h = k_F^S \sqrt{1 - \frac{e^2 - \Delta_0^2}{(E_F^S)^2}}. \quad (\text{A3})$$

In the normal regions where the gap function is zero the wave vectors q_p and q_h are now

$$q_p = k_F \sqrt{1 + \frac{e}{E_F^N}} \quad \text{and} \quad q_h = k_F \sqrt{1 - \frac{e}{E_F^N}}. \quad (\text{A4})$$

Note that high- T_c materials often have anisotropic order parameters, for example the cuprate LSCO we used as a model system has a d-wave order parameter of the form $\Delta(\theta) = \Delta_0 \cos(2(\theta - \alpha))$, where θ is the direction of travel through the crystal with respect to the orientation of the lattice α [38]. We make the standard approximation that the gap function can be modeled using a step function. Generally speaking the gap function of a superconducting heterostructure needs to be evaluated self-consistently and the validity of this step function approximation is addressed in detail in [41] and [42].

Previous theoretical work has been done on the effect treating the gap function self-consistently on the predicted behavior of superconducting heterostructures. Some of the earliest work is by McMillan, who used Greens functions methods to calculate the first-order corrections to the step-function approximation [43]. In [44], van Son, van Kempen, and Wyder used a qualitative model for the self-consistent gap function and found a dampening of geometrical oscillations in the transmission through an NINS tunnel junction. Martin and Lambert self-consistently calculated the gap function for the NSN structure and calculated corrections to the differential conductance of the system [45], finding the most significant corrections at bias voltages comparable to and larger than the maximum gap energy Δ_0 . Comparable findings to those of [45] were by Sánchez-Cañizares and Sols [46–48].

APPENDIX B: ELECTRON FIELD OPERATOR

In this Appendix we give the field operator for excitations in a single transverse mode coming initially from the thermal reservoir attached to the left lead [18],

$$\hat{\psi}_{N_L}(z, t) = \begin{pmatrix} \hat{\psi}_{N_L}^p \\ \hat{\psi}_{N_L}^h \end{pmatrix}, \quad (\text{B1})$$

where

$$\hat{\psi}_{N_L}^p = \sqrt{\frac{1}{2\pi} \frac{m_L}{\hbar^2}} e^{-iE_F t/\hbar} \int_0^{\epsilon_{\max}} de \left[\frac{1}{\sqrt{q_p^L}} e^{-iet/\hbar} \left(\hat{a}_{e,p}^L e^{iq_p^L z} + r_{pp}^{LL} \hat{a}_{e,p}^L e^{-iq_p^L z} + t_{pp}^{LR} \hat{a}_{e,p}^R e^{-iq_p^L z} + r_{ph}^{LL} \hat{a}_{e,h}^L e^{-iq_p^L z} + t_{ph}^{LR} \hat{a}_{e,h}^R e^{-iq_p^L z} \right) \right], \quad (\text{B2})$$

$$\hat{\psi}_{N_L}^h = \sqrt{\frac{1}{2\pi} \frac{m_L}{\hbar^2}} e^{-iE_F t/\hbar} \int_0^{\epsilon_{\max}} de \left[\frac{1}{\sqrt{q_h^L}} e^{+iet/\hbar} \left(\hat{a}_{e,h}^L e^{-iq_h^L z} + r_{hp}^{LL} \hat{a}_{e,p}^L e^{iq_h^L z} + t_{hp}^{LR} \hat{a}_{e,p}^R e^{iq_h^L z} + r_{hh}^{LL} \hat{a}_{e,h}^L e^{iq_h^L z} + t_{hh}^{LR} \hat{a}_{e,h}^R e^{iq_h^L z} \right) \right]. \quad (\text{B3})$$

Here, $\epsilon_{\max} = \frac{E^{\text{tr}}}{2}$ is the maximum energy of the particular transverse mode we are restricted to. The annihilation operators, $\hat{a}_{e,\beta}^{\alpha}$, annihilate an excitation of type $\beta \in \{p, h\}$ in the α^{th} normal lead ($\alpha \in \{L, R\}$) with energy e , with the same convention used for the creation operators. For holes our convention for the energy label denotes how far below the Fermi energy the excitation is, and thus is a positive value. In the field operators we have explicitly included all of the different scattering channels that give rise to excitations moving in the $-z$ direction.

APPENDIX C: EXPRESSIONS FOR SCATTERING COEFFICIENTS AND NOISE USING THE ANDREEV APPROXIMATION

In Eqs. (C1) and (C2) below we give the expressions for t_{pp}^{RL} and t_{hh}^{RL} , respectively, using the Andreev approximation:

$$t_{pp}^{RL} = -\frac{(u-v)^2(u+v)^2 e^{i((h_2+h_4)(k_h+k_p)+h_3(q_h+q_p)-h_4q_p)}}{\text{Den}_{pp}}, \quad (\text{C1})$$

$$t_{hh}^{RL} = -\frac{(u-v)^2(u+v)^2 e^{i(h_2(q_h+q_p)+h_3(k_h+k_p)+h_4q_h+\phi)}}{\text{Den}_{hh}}, \quad (\text{C2})$$

$$\begin{aligned} \text{Den}_{pp} = & u^2 v^2 (e^{i(h_2k_h)} - e^{i(h_2k_p)})(e^{i(h_3k_p+h_4k_h)} - e^{i(h_3k_h+h_4k_p)})e^{i(h_2q_h+h_3q_p+\phi)} \\ & - e^{i(h_2q_p+h_3q_h)}(u^2 e^{i(h_2k_h)} - v^2 e^{i(h_2k_p)})(u^2 e^{i(h_3k_p+h_4k_h)} - v^2 e^{i(h_3k_h+h_4k_p)}), \end{aligned} \quad (\text{C3})$$

$$\begin{aligned} \text{Den}_{hh} = & u^2 v^2 (e^{i(h_2k_h)} - e^{i(h_2k_p)})(e^{i(h_3k_p+h_4k_h)} - e^{i(h_3k_h+h_4k_p)})e^{i(h_2q_h+h_3q_p)} \\ & - e^{i(h_2q_p+h_3q_h+\phi)}(u^2 e^{i(h_2k_h)} - v^2 e^{i(h_2k_p)})(u^2 e^{i(h_3k_p+h_4k_h)} - v^2 e^{i(h_3k_h+h_4k_p)}). \end{aligned} \quad (\text{C4})$$

The expressions for the different contributions to the cross-correlated shot noise also simplify under the Andreev approximation due to the setting of $r_{pp}^{LL} = r_{hh}^{LL} = r_{pp}^{RR} = r_{hh}^{RR} = 0$ and $t_{hp}^{LR} = t_{ph}^{LR} = t_{hp}^{RL} = t_{ph}^{RL} = 0$:

$$S_{pp}^{LR} = \frac{m_L m_R}{\pi^2 \hbar^4} \int de [F_p^L N_p^L (-|r_{hp}^{LL}|^2 - 1) |t_{pp}^{RL}|^2 + F_p^R N_p^R + p(-|r_{hp}^{RR}|^2 - 1) |t_{pp}^{LR}|^2], \quad (\text{C5})$$

$$S_{hh}^{LR} = \frac{m_L m_R}{\pi^2 \hbar^4} \int de [F_h^L N_h^L (-|r_{ph}^{LL}|^2 - 1) |t_{hh}^{RL}|^2 + F_h^R N_h^R (-|r_{ph}^{RR}|^2 - 1) (|t_{hh}^{LR}|^2)], \quad (\text{C6})$$

$$S_{ph}^{LR} = \frac{m_L m_R}{\pi^2 \hbar^4} \int de [- (F^L N^R + F^R N^L) (\text{Re}[r_{ph}^{LL*} r_{hp}^{RR*} t_{hh}^{RL} t_{pp}^{LR}] + \text{Re}[r_{hp}^{LL*} r_{ph}^{RR*} t_{pp}^{RL} t_{hh}^{LR}])]. \quad (\text{C7})$$

-
- [1] J. C. Gil, S. Gomez P., and W. J. Herrera, *Solid State Commun.* **258**, 25 (2017).
[2] M. Veldhorst and A. Brinkman, *Phys. Rev. Lett.* **105**, 107002 (2010).
[3] P. Burset, W. J. Herrera, and A. L. Yeyati, *Phys. Rev. B* **84**, 115448 (2011).
[4] J. Schindele, A. Baumgartner, and C. Schönenberger, *Phys. Rev. Lett.* **109**, 157002 (2012).
[5] L. Hofstetter, S. Csonka, J. Nygård, and C. Schönenberger, *Nature (London)* **461**, 960 (2009).
[6] J. Linder and J. W. Robinson, *Nat. Phys.* **11**, 307 (2015).
[7] M. Eschrig, *Rep. Prog. Phys.* **78**, 104501 (2015).
[8] S. Das Sarma, J. Fabian, Xuedong Hu, and I. Zutic, *IEEE Trans. Magn.* **36**, 2821 (2000).
[9] H.-A. Engel, P. Recher, and D. Loss, *Solid State Commun.* **119**, 229 (2001).
[10] F. Keidel, S.-Y. Hwang, B. Trauzettel, B. Sothmann, and P. Burset, *Phys. Rev. Research* **2**, 022019(R) (2020).
[11] N. M. Chtchelkatchev, G. Blatter, G. B. Lesovik, and T. Martin, *Phys. Rev. B* **66**, 161320(R) (2002).
[12] G. Bignon, M. Houzet, F. Pistolesi, and F. Hekking, *Europhys. Lett.* **67**, 110 (2004).
[13] A. L. Yeyati, F. Bergeret, A. Martin-Rodero, and T. Klapwijk, *Nat. Phys.* **3**, 455 (2007).
[14] A. Freyn, M. Flöser, and R. Mélin, *Phys. Rev. B* **82**, 014510 (2010).
[15] D. S. Golubev and A. D. Zaikin, *Phys. Rev. B* **99**, 144504 (2019).
[16] L. G. Herrmann, F. Portier, P. Roche, A. L. Yeyati, T. Kontos, and C. Strunk, *Phys. Rev. Lett.* **104**, 026801 (2010).
[17] L. Hofstetter, S. Csonka, A. Baumgartner, G. Fülöp, S. d'Hollosy, J. Nygård, and C. Schönenberger, *Phys. Rev. Lett.* **107**, 136801 (2011).
[18] C. Ostrove and L. E. Reichl, *Phys. B* **561**, 79 (2019).
[19] X.-L. Huang and Y. V. Nazarov, *Phys. Rev. B* **100**, 155411 (2019).
[20] V. Bouchiat, N. Chtchelkatchev, D. Feinberg, G. Lesovik, T. Martin, and J. Torres, *Nanotechnology* **14**, 77 (2002).
[21] G. Deutscher, *J. Supercond.* **15**, 43 (2002).
[22] G. Deutscher and D. Feinberg, *Appl. Phys. Lett.* **76**, 487 (2000).
[23] D. Chevallier, J. Rech, T. Jonckheere, and T. Martin, *Phys. Rev. B* **83**, 125421 (2011).
[24] J. Cayssol, *Phys. Rev. Lett.* **100**, 147001 (2008).
[25] I. Borzenets, Y. Shimazaki, G. Jones, M. F. Craciun, S. Russo, M. Yamamoto, and S. Tarucha, *Sci. Rep.* **6**, 23051 (2016).
[26] S. K. Firoz Islam and A. Saha, *Phys. Rev. B* **96**, 125406 (2017).
[27] G. Fülöp, S. d'Hollosy, A. Baumgartner, P. Makk, V. A. Guzenko, M. H. Madsen, J. Nygård, C. Schönenberger, and S. Csonka, *Phys. Rev. B* **90**, 235412 (2014).

- [28] G. Fülöp, F. Domínguez, S. d'Hollosy, A. Baumgartner, P. Makk, M. H. Madsen, V. A. Guzenko, J. Nygård, C. Schönenberger, A. Levy Yeyati, and S. Csonka, *Phys. Rev. Lett.* **115**, 227003 (2015).
- [29] P. Trocha and I. Weymann, *Phys. Rev. B* **91**, 235424 (2015).
- [30] P. Trocha and K. Wrzeźniewski, *J. Phys.: Condens. Matter* **30**, 305303 (2018).
- [31] K. Wrzeźniewski, P. Trocha, and I. Weymann, *J. Phys.: Condens. Matter* **29**, 195302 (2017).
- [32] P. Busz, D. Tomaszewski, and J. Martinek, *Phys. Rev. B* **96**, 064520 (2017).
- [33] P.-G. de Gennes, *Superconductivity of Metals and Alloys* (CRC Press, Boca Raton, 2018).
- [34] J. Demers and A. Griffin, *Can. J. Phys.* **49**, 285 (1971).
- [35] G. E. Blonder, M. Tinkham, and T. M. Klapwijk, *Phys. Rev. B* **25**, 4515 (1982).
- [36] C. Beenakker, in *Transport Phenomena in Mesoscopic Systems* (Springer, Berlin, 1992) pp. 235–253.
- [37] A. Andreev, *Zh. Eksp. Teor. Fiz.* **47**, 2222 (1965) [*Sov. Phys. JETP* **20**, 1490 (1965)].
- [38] M. Cyrot and D. Pavuna, *Introduction to Superconductivity and High-Tc Materials* (World Scientific, Singapore, 1992).
- [39] M. Flöser, From local to non-local transport: Percolation in quantum hall systems, cross-correlations in superconducting hybrid structures, Ph.D. thesis, The University of Grenoble, 2012.
- [40] M. Stehno, Investigations of nonlocal transport and current noise in mesoscopic normal metal-superconductor hybrid structures, Ph.D. thesis, University of Illinois at Urbana-Champaign, 2013.
- [41] K. Likharev, *Rev. Mod. Phys.* **51**, 101 (1979).
- [42] M. Y. Kupriyanov and V. Lukichev, *Fiz. Nizk. Temp.* **8**, 1045 (1982).
- [43] W. McMillan, *Phys. Rev.* **175**, 559 (1968).
- [44] P. C. van Son, H. van Kempen, and P. Wyder, *Phys. Rev. B* **37**, 5015 (1988).
- [45] A. Martin and C. J. Lambert, *Phys. Rev. B* **51**, 17999 (1995).
- [46] J. Sánchez-Canizares and F. Sols, *Phys. Rev. B* **55**, 531 (1997).
- [47] J. Sánchez-Cañizares and F. Sols, *Phys. B: Condens. Matter* **252**, 304 (1998).
- [48] J. Sanchez-Canizares and F. Sols, *J. Low Temp. Phys.* **122**, 11 (2001).